Journal of Alzheimer's Disease 72 (2019) 1323–1339
DOI 10.3233/JAD-181190
IOS Press



# Parvalbumin-Positive Neuron Loss and Amyloid-β Deposits in the Frontal Cortex of Alzheimer's Disease-Related Mice

Farhan Ali[a,*], Stephanie L. Baringer[b], Arianna Neal[a], Esther Y. Choi[a] and Alex C. Kwan[a,c]
[a]*Department of Psychiatry, Yale University School of Medicine, New Haven, CT, USA*
[b]*Department of Psychology, University of New Haven, New Haven, CT, USA*
[c]*Department of Neuroscience, Yale University School of Medicine, New Haven, CT, USA*

Handling Associate Editor: Oliver Wirths

Accepted 7 October 2019

**Abstract**. Alzheimer's disease (AD) has several hallmark features including amyloid-β (Aβ) plaque deposits and neuronal loss. Here, we characterized Aβ plaque aggregation and parvalbumin-positive (PV) GABAergic neurons in 6–9-month-old 5xFAD mice harboring mutations associated with familial AD. We used immunofluorescence staining to compare three regions in the frontal cortex—prelimbic (PrL), cingulate (Cg, including Cg1 and Cg2), and secondary motor (M2) cortices—along with primary somatosensory (S1) cortex. We quantified the density of Aβ plaques, which showed significant laminar and regional vulnerability. There were more plaques of larger sizes in deep layers compared to superficial layers. Total plaque burden was higher in frontal regions compared to S1. We also found layer- and region-specific differences across genotype in the density of PV interneurons. PV neuron density was lower in 5xFAD mice than wild-type, particularly in deep layers of frontal regions, with Cg (–50%) and M2 (–39%) exhibiting the largest reduction. Using *in vivo* two-photon imaging, we longitudinally visualized the loss of frontal cortical PV neurons across four weeks in the AD mouse model. Overall, these results provide information about Aβ deposits and PV neuron density in a widely used mouse model for AD, implicating deep layers of frontal cortical regions as being especially vulnerable.

Keywords: 5xFAD, amyloid-β, cingulate cortex, familial Alzheimer's disease, frontal cortex, parvalbumin-positive neurons, plaques, secondary motor cortex

## INTRODUCTION

Alzheimer's disease (AD), a major cause of dementia, is characterized at the microscopic level by deposits of intracellular neurofibrillary tangles made up of hyperphosphorylated tau and extracellular plaques consisting of an amyloid-β (Aβ) peptide core. There are significant regional differences in vulnerability to Aβ plaques in the brains of AD patients. Based on postmortem work, association cortices show initial vulnerability followed by primary motor and sensory regions [1, 2]. More recent positron emission tomography imaging of living patients using Aβ binding dyes have corroborated postmortem findings of regional differences in Aβ deposits [3, 4]. Concomitant with the Aβ plaque deposits is neuronal loss. Neurodegeneration also exhibits differences in regional vulnerability based on postmortem reports [5] and structural imaging of grey matter in living patients [6]. Multiple studies have reported relations between Aβ plaques and neuronal loss, as well as regional specificity of this relationship [7–10].

*Correspondence to: Farhan Ali, Department of Psychiatry, Yale University School of Medicine, 300 George St., Suite 901, New Haven, CT 06511, USA. Tel.: +1 203 785 6396; E-mail: farhan.ali@yale.edu.

However, much less is known about the impact of amyloid pathology on GABAergic neurons in the neocortex. Several lines of evidence suggest GABAergic neurons are impacted by AD. GABA concentrations [11] and GABA receptor density [12] are reduced in AD brain specimens, findings supported by neuroimaging studies using GABA receptor ligands [13, 14]. More direct evidence of GABAergic neuronal alterations has come from staining of GABAergic neurons. GABAergic neurons are diverse and can be classified into subtypes [15]. One prominent subtype is the parvalbumin-expressing (PV) cells, which innervate the soma of pyramidal neurons to provide powerful inhibition of spiking activity. Postmortem staining of PV neurons has found significant reduction in PV neuron density in the cerebral cortex of AD patients compared to healthy subjects in some studies [16–18], but not others [19, 20]. Most PV staining studies have not examined AD-related lesions in the same tissues to correlate with the PV neuron loss. In one notable exception, a study reported that loss of PV neurons in the entorhinal cortex was correlated with a combined measure of AD pathology comprising of neurofibrillary tangles and Aβ plaques: higher AD pathology was associated with lower density of PV neurons in patients [21]. However, it is not clear if there is correlation between PV neuron loss with Aβ plaques specifically in other parts of the brain.

Transgenic mice are useful models to better understand the pathophysiological processes underlying AD [22]. One widely used transgenic model is the 5xFAD mouse [23]. These mice harbor familial AD-related mutations in the transgenes encoding amyloid-β protein precursor (AβPP) and presenilin-1 (PS1). The five mutations in the transgenes produce an aggressive overexpression of Aβ peptides, leading to Aβ plaque deposits from as early as 2 months of age [23]. AD-related phenotypes have been extensively described for the 5xFAD mouse model, including neuronal density [24, 25], synaptic markers [23], dendritic spines [26], axonal structures [27, 28], and cognitive behaviors [29, 30]. However, a comparative analysis of PV neurons and its relation to Aβ plaques in the 5xFAD model has been lacking.

To address these knowledge gaps, here we use immunostaining of 5xFAD brain sections to characterize the distribution of Aβ aggregation in different parts of the neocortex with emphasis on the frontal regions. We investigate whether there is loss of PV interneurons in 5xFAD mice compared to wild-type (WT) controls in these regions. We assess potential differences between cortical layers in these two factors. Finally, we examine any correlation between Aβ aggregation and PV neurons density across regions.

## MATERIALS AND METHODS

### *Animals*

We used male hemizygous 5xFAD mice (Jackson Laboratory Stock No. 006554, also known as MMRRC Stock No. 34840-JAX), which overexpress transgenes with the K670 N/M671 L (Swedish), I716 V (Florida), and V717I (London) mutations in human AβPP gene, as well as M146 L and L286 V mutations in human presenilin-1 gene under the mouse Thy1 promoter [23]. We mated male 5xFAD transgenic mice with female C57BL/6J WT strain (Jackson Laboratory Stock No. 000664) to obtain 5xFAD transgenic animals and WT littermate controls. For *in vivo* imaging experiments, we crossed hemizygous 5xFAD mice with homozygous PV-IRES-Cre mice [31] (Jackson Laboratory Stock No 008069), producing animals that were heterozygous for Cre and either positive for 5xFAD (5xFAD/PV-Cre) or negative (PV-Cre, control littermates). Genotyping was done with polymerase chain reaction using recommended primers and protocol for the mouse line. Transgenic 5xFAD mice at 6–9 months in age together with their age-matched WT littermate controls were used for histology. We chose this age range because initial characterizations indicated that mice at this age exhibited significant Aβ plaque deposits with some general neuronal loss as indicated by Nissl staining [23]. All experimental procedures were approved by the Institutional Animal Care and Use Committee, Yale University.

### *Immunostaining*

Mice were sacrificed by transcardial perfusion of phosphate-buffered saline (PBS) followed by paraformaldehyde (PFA) solution (4% (v/v) in PBS). The brain was harvested and stored in PFA solution for 24–48 h at 4°C before being transferred to PBS. Coronal sections (100 μm-thick) were sliced with a vibratome. Sections containing prelimbic (PrL), cingulate (Cg), secondary motor (M2), and primary somatosensory (S1) cortices (Fig. 1A-D) were immediately used for staining. Cg included both Cg1 and Cg2 in the mouse brain atlas [32]. PV staining was done free-floating with the following protocol: antigen retrieval in 1x citrate buffer, pH 6.0 (Abcam

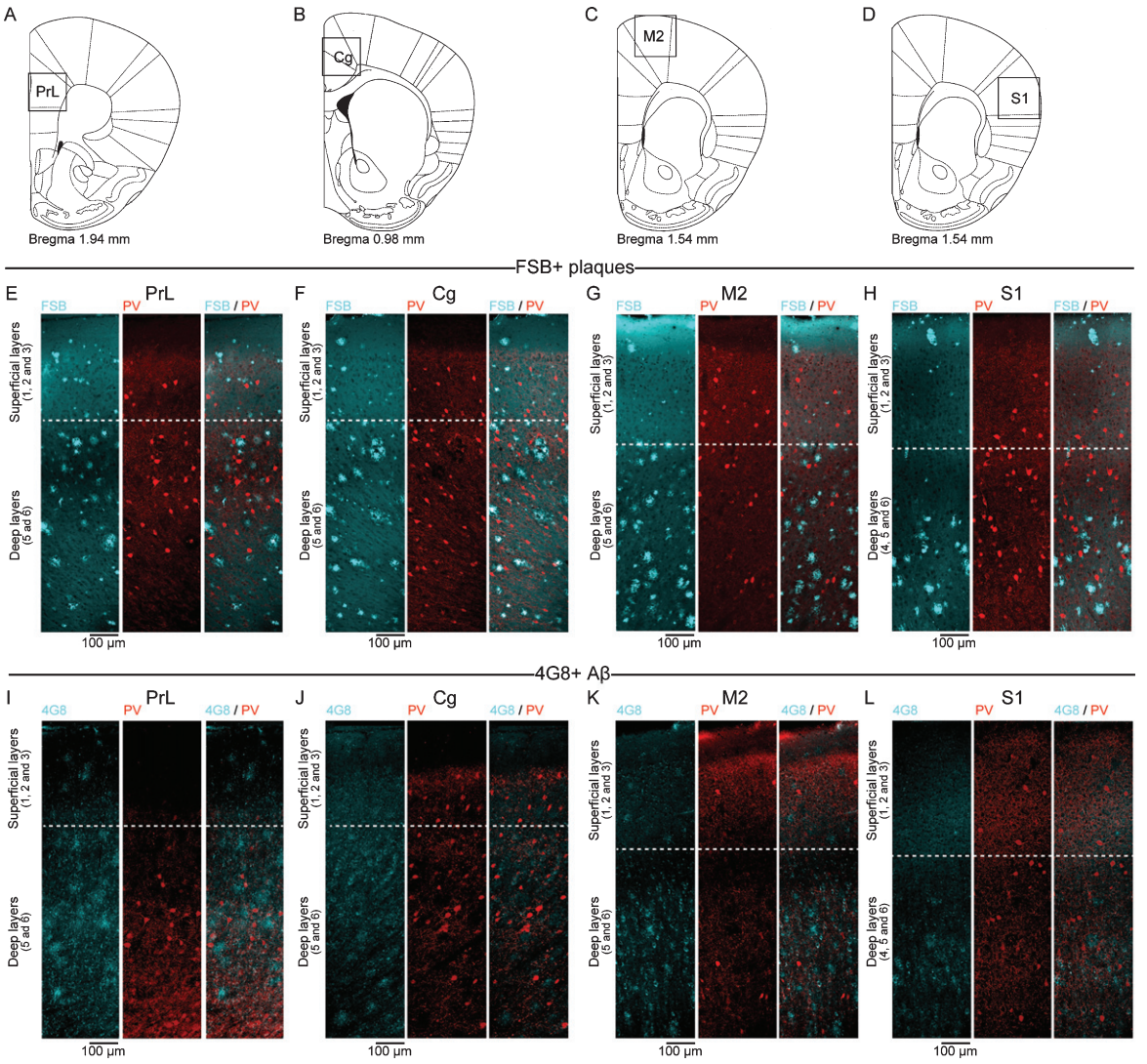


Fig. 1. FSB, 4G8, and PV stains in four regions of the neocortex in 5xFAD mice. A-D) Brain atlases showing coronal sections of four regions examined in the study: prelimbic cortex (PrL), cingulate cortex (Cg, including Cg1 and Cg2), secondary motor cortex (M2), and primary somatosensory cortex (S1). Boxes, approximate (1.1 × 1.1 mm) regions imaged and analyzed. Brain atlases taken from [32]. E) Example FSB (left), PV (middle), and composite image of the two stains (right) in a coronal section of PrL from a 5xFAD mouse. F-H) Same as (E) but for Cg, M2, and S1. I) Example 4G8 (left), PV (middle), and composite image of the two stains (right) in a coronal section of PrL from a 5xFAD mouse. J-L) Same as (I) for but Cg, M2, and S1. White dotted line, boundary separating superficial layers (1, 2, and 3) and deep layers (5 and 6 or 4, 5, and 6) estimated using the Allen Mouse Common Coordinate Framework version 3.

ab64214) for 20 min at 70°C followed by blocking (PBS with 0.5% Triton and 5% goat serum) for 1 h at room temperature (RT) followed by primary antibody incubation (rabbit polyclonal to PV, Abcam ab11427, 1:1000) for at least 12 h at 4°C. The specificity of the primary antibody to parvalbumin has been previously validated [33–35]. After the primary antibody, we did secondary antibody incubation (goat anti-rabbit IgG-Alexa Fluor 555, Abcam ab150078; 1:500) for 3 h at RT. To stain for Aβ plaques, we then incubated the sections in the FSB dye (1:3000 from original stock of 5 mg/ml; MilliporeSigma 344101) for 30 min at RT. To stain other forms of Aβ aggregation, we used the anti-Aβ antibody 4G8. This antibody recognizes an epitope that can potentially cross-react with precursor forms including AβPP. However, a previous study found that sections pre-treated with heat combined with formic acid led to 4G8 staining that was distinct from AβPP [36]. We followed this pretreatment for our 4G8 staining in a sepa-

rate cohort of animals: antigen retrieval in 1x citrate buffer, pH 6.0 (Abcam ab64214) for 45 min at 95°C followed by successive incubations in 88% formic acid (20 min at RT), blocking solution (1 h at RT) and primary antibody incubation (mouse anti-rabbit Aβ monoclonal to amyloid-β, Biolegend 800712, clone 4G8; 1:1000; at least 12 h at 4°C). After primary antibody incubation, the sections were then placed in secondary antibody (goat anti-mouse IgG-Alexa Fluor 488, Abcam ab150117; 1:500; 3 h at RT). We washed the sections with PBS for 3 times in between all change of reagents for all staining. The sections were finally washed with filtered $H_2O$ before being air-dried, mounted on slides and sealed with coverslips using DPX mounting medium (MilliporeSigma 06522) for long-term storage [37]. We performed all perfusion, slicing, and staining in batches of 3–5 animals consisting of sections from both 5xFAD and WT animals.

*Confocal imaging*

We used a confocal laser scanning microscope (Olympus FV1000) and its accompanying software for all imaging. Under widefield fluorescence mode, we first identified the four regions to be imaged using landmarks such as white matter and ventricles. After delineating the area to be imaged, the lasers for FSB (405 nm), 4G8 (473 nm), and PV (559 nm) staining were turned on for confocal imaging. We took partially overlapping images (800 × 800 pixels/image, 0.795 μm/pixel) that tiled the brain region of interest, using a 20x objective with a focal plane at approximately 10 μm deep into the brain section. We used the same laser power and photodetector settings for all images taken.

*Histological analysis*

We stitched the partially overlapping images from each fluorescence detection channel to form a larger field of view using an ImageJ stitching plugin [38]. The stitched images were separately analyzed for labeling of FSB, 4G8, and PV. The fluorescence channel corresponding to FSB staining of Aβ plaques was analyzed in a two-step process. The first step involved identifying Aβ plaques based on morphology and brightness of fluorescent signals compared to background (Supplementary Figure 1A, left). A region of interest (ROI) encompassing each identified Aβ plaque was manually drawn using the freehand selection tool in ImageJ. This hand-drawn ROI was made to trace the most exterior perimeter of the plaque structure, keeping in mind that the second step would refine and classify the pixels in a more unbiased, automated manner. For the second step, the hand-drawn ROIs (Supplementary Figure 1A, middle) along with the original fluorescence image were imported into MATLAB (Mathworks). For each plaque, a background ROI was estimated by calculating $r$, the radius of a circle if the hand-drawn ROI area was considered as the area of a circle, and then creating a background ROI which was a circle with a radius of $3r$, excluding pixels belonging to the hand-drawn ROI itself as well as overlapping hand-drawn ROIs of other nearby plaques. A threshold was calculated as two times the standard deviation above the mean of values of all the pixels within the background ROI. From the hand-drawn ROI, pixels above the threshold were kept to generate the final ROI for a plaque, henceforth labeled as "FSB+ plaques" (Supplementary Figure 1A, right). This process was repeated for all of the plaques identified in the first step. This two-step procedure for analyzing plaques provides a consistent way to compute plaque area and reduces human bias.

For 4G8 staining, we used a fully automated analysis due to the extensive amount of staining including small puncta, which precluded manual segmentation. We first imported the stitched images corresponding to the 4G8 Aβ channel from all animals into MATLAB. We then computed the 95$^{th}$ percentile of the histogram of all pixel values from all the imported images. Pixels with values above this threshold were kept, henceforth labeled as "4G8+ Aβ" while the rest of the pixels were given values of 0 (Supplementary Figure 1B). To segment the pixels into separate ROIs, we then used the function 'bwconncomp' in MATLAB. Above-threshold pixels connected to other above-threshold pixels via any of the 4 sides or 4 edges of the square pixels (8-connected algorithm) were considered part of the same 4G8+ Aβ ROI. In an additional analysis, we excluded intracellular 4G8 staining to rule out potential confounds of intracellular AβPP staining. We manually drew masks over the 4G8 Aβ channel by identifying donut-shaped staining as a proxy for intracellular staining. These masks were then used to exclude intracellular 4G8+ staining for further analysis.

For PV neurons, we manually drew ROIs using the freehand selection tool in ImageJ (Supplementary Figure 1C). All PV neuron ROIs were drawn blind to both genotype, and the FSB and 4G8+ Aβ channels. To quantify the fluorescence, for each neuron, we computed a corresponding local background

mask similar to the plaque approach above: assuming a circle with the same area as the neuron and drawing a larger circle with radius of *3r*, excluding pixels overlapping with nearby neurons. We then divided the average fluorescence in the neuron by the average fluorescence in the local background mask for a normalized measure of PV neuron fluorescence.

Further analyses of the ROIs for each channel were subsequently performed in MATLAB. Centroid location of each ROI was computed using the 'regionprops' function. Each plaque and PV ROI was then assigned to either superficial (layers 1, 2, and 3) or deep (layers 5 and 6 for frontal regions and layers 4, 5, and 6 for S1) layers based on its distance from the cortical surface. The approximate distance from the cortical surface to delineate the boundary between superficial and deep layers for each region was taken from the Allen Mouse Common Coordinate Framework version 3 (PrL, 350 μm; Cg, 350 μm; M2, 450 μm; S1, 470 μm). FSB+ plaque and 4G8+ Aβ sizes were computed by counting the number of above-threshold pixels in the final ROI and converting it to $\mu m^2$ based on the area of each pixel (0.795 μm × 0.795 μm). Total plaque and 4G8+ Aβ area (%) was calculated by dividing the sum of ROI areas by the total area of tissue analyzed.

### *In vivo imaging*

To complement the histological findings, we performed longitudinal *in vivo* two-photon imaging using 5xFAD/PV-Cre animals. The PV-IRES-Cre mice have a knocked-in *cre* sequence to 3' UTR of exon 5 of the *Pvalb* gene, with expression of Cre recombinase driven by endogenous *Pvalb* promoter. We crossed hemizygous 5xFAD mice with homozygous PV-IRES-Cre mice [31], producing animals that were heterozygous for Cre and either positive for 5xFAD (5xFAD/PV-Cre) or negative (PV-Cre, control littermates). At ∼6 months of age, we injected these animals with an adeno-associated viral vector (AAV.Syn.Flex.NES-jRGECO1a.WPRE.SV40, Addgene 100853-AAV1) for Cre-dependent expression of jRGECO1a, a red-shifted calcium indicator [39], in PV neurons in Cg1 and M2. Three weeks later, a larger craniotomy was performed to chronically implant a glass window over the injection sites, allowing optical access of the brain for two-photon microscopy. Details of injection and cranial window surgeries have been previously described in detail [40].

We performed *in vivo* imaging about 2 weeks after cranial window surgery. The animal was awake and head-fixed under a laser-scanning two-photon microscope (Movable Objective Microscope, Sutter Instrument) with a water immersion objective (XLUMPLFLN, 20X/0.95 N.A., Olympus), controlled by the ScanImage software [41]. The excitation was provided by a Ti:Sapphire femotosecond laser (Chameleon Ultra II, Coherent) tuned to 980 nm. For each animal, we identified up to 8 fields of view, each with 1 to 9 jRGECO1a-expressing PV neurons, at a depth of between 150 and 450 μm relative to the surface of the brain. Fluorescence was collected behind a filter centering at 624 nm and by a GaAsP photomultiplier tube. Images (128 × 128 or 256 × 256; 1.35 μm per pixel) were obtained at 3 imaging timepoints, with each timepoint separated by 2 weeks. We used the pattern of neuronal labeling and other structural features (e.g., blood vessels which appeared as dark structures) to return to the same field of view. The images were then analyzed offline for presence/absence of PV neurons by an assistant blinded to the genotype of the animals. We have labeled the cells using a calcium indicator, jRGECO1a, because of a separate study on activity dynamics of PV neurons (data not shown here). Even though the jRGECO1a signal is activity-dependent, it is suitable for detecting the presence of PV neurons because the cells have high spontaneous firing rates and each cell is imaged for at least 10 min.

### *Statistics*

For statistical comparisons, we used parametric ANOVA for factorial designs for each of the layers followed by parametric *post-hoc* tests. For FSB+ plaque and 4G8+ Aβ areas, because the distributions were non-normal (Fig. 2C, 2D, 3C, 3D), we used non-parametric Kruskal-Wallis ANOVA for each of the layers followed by non-parametric *post-hoc* tests. All statistical tests were two-tailed with $\alpha = 0.05$. In the figures, *p*-values were represented as $*p < 0.05$; $**p < 0.01$. See main text for exact *p*-values.

## RESULTS

We imaged and analyzed, on average, an area of 1.21 $mm^2$ of brain tissue for each of the 4 regions including PrL, Cg, M2, and S1 in each animal (Fig. 1A-D). Figure 1E-L shows example FSB, 4G8, and PV staining in the four regions. FSB, an analog

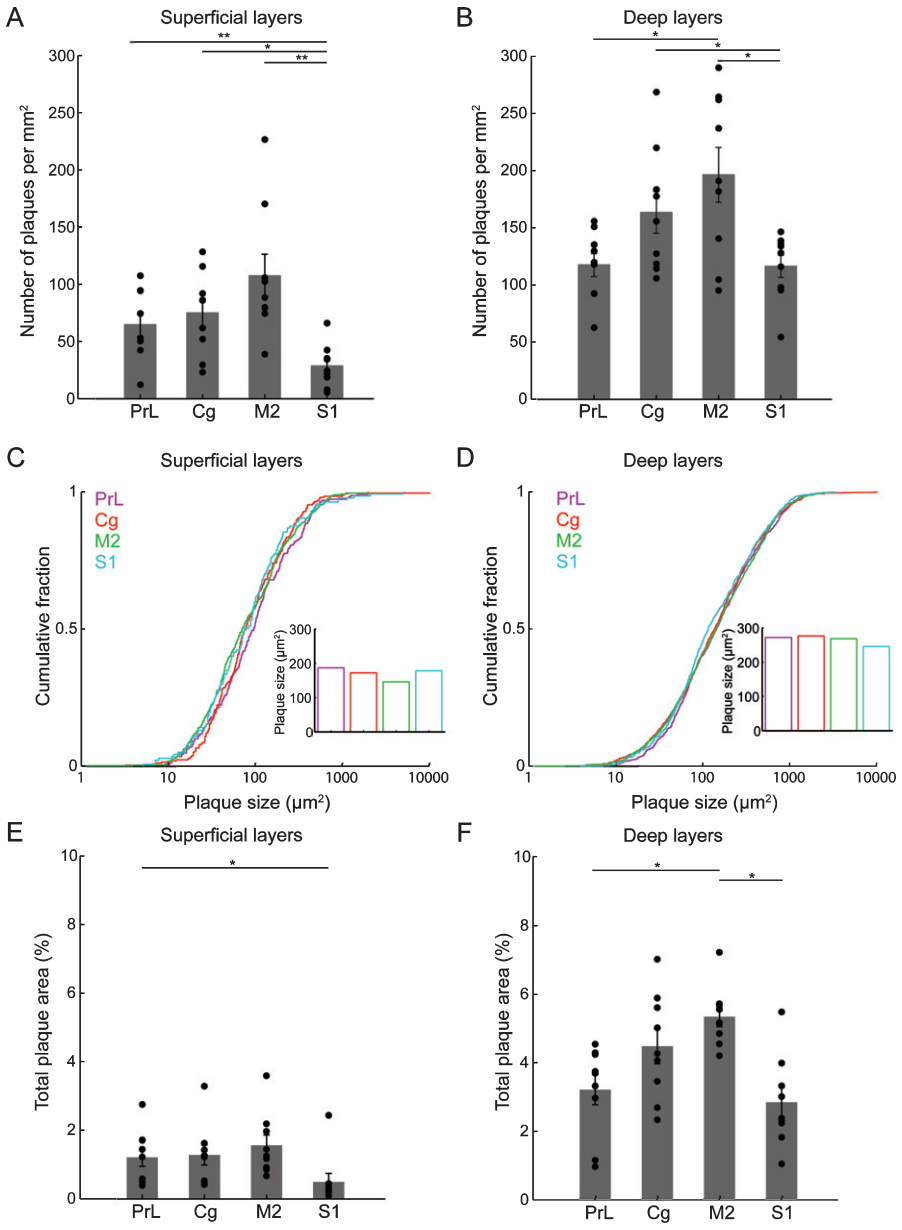


Fig. 2. Laminar and regional distribution of FSB+ plaques. A) Number of FSB+ plaques per mm$^2$ of superficial layers in each brain region examined. B) Same as (A) but for deep layers. C) Cumulative fraction of absolute size of all FSB+ plaques (log10-transformed) analyzed as a function of superficial layers in each brain region examined. Inset, mean FSB+ plaque size. D) Same as (C) but for deep layers. E) Total FSB+ plaque area as a percentage of superficial layers in each brain region examined. F) Same as (E) but for deep layers. Filled circle, individual animal. Bar, mean ± s.e.m. *$p < 0.05$; **$p < 0.01$.

of Congo Red and BSB, is an Aβ binding dye that selectively and brightly labels the enriched β-sheet structures in Aβ plaques [42]. 4G8 is an anti-Aβ antibody that recognizes an epitope corresponding to amino acid residues 18–23 of the Aβ peptide [43]. The antibody has been shown to label various forms and sizes of Aβ including oligomeric Aβ [44], allowing us to investigate non-plaque species of Aβ aggregation to complement the FSB staining.

### *FSB+ plaques*

We first examined the characteristics of FSB+ plaques across the different regions in 5xFAD ani-

mals. For superficial layers, there were regional differences in the density of FSB+ plaques: PrL, $65 \pm 10$ plaques per $mm^2$ (mean $\pm$ SEM); Cg, $75 \pm 12$ plaques per $mm^2$; M2, $107 \pm 19$ plaques per $mm^2$; S1, $29 \pm 6$ plaques per $mm^2$ (Fig. 2A). All three frontal regions had statistically significantly higher density of plaques compared to S1 (One-way ANOVA with brain region as a within subjects factor, $F(3) = 10.6$, $p = 1 \times 10^{-4}$. *Post-hoc* Tukey-Kramer tests: PrL versus Cg, $p = 0.85$; PrL versus M2, $p = 0.22$; PrL versus S1, $p = 0.006$; Cg versus M2, $p = 0.09$; Cg versus S1, $p = 0.02$; M2 versus S1, $p = 0.009$). For deep layers, there was also a statistically significant regional effect with M2 exhibiting the highest count of plaques: PrL, $117 \pm 10$ plaques per $mm^2$; Cg, $164 \pm 18$ plaques per $mm^2$; M2, $197 \pm 24$ plaques per $mm^2$; S1, $116 \pm 10$ plaques per $mm^2$ (Fig. 2B; One-way ANOVA with brain region as a within subjects factor, $F(3) = 10.4$, $p = 1 \times 10^{-4}$. *Post-hoc* Tukey-Kramer tests: PrL versus Cg, $p = 0.09$; PrL versus M2, $p = 0.01$; PrL versus S1, $p = 0.99$; Cg versus M2, $p = 0.46$; Cg versus S1, $p = 0.03$; M2 versus S1, $p = 0.01$).

Sizes of individual plaques vary, spanning over three orders of magnitude. The distribution was non-normal and heavy-tailed: there were many small plaques and fewer large plaques (Fig. 2C, D; note the log-transformed x-axis). There was no statistically significant effect of region in the superficial layers (Fig. 2C; PrL, $187 \pm 2\ \mu m^2$, $n = 228$ plaques; Cg, $172 \pm 3\ \mu m^2$, $n = 255$ plaques; M2, $146.0 \pm 0.4\ \mu m^2$, $n = 495$ plaques; S1, $178 \pm 3\ \mu m^2$, $n = 137$ plaques; Non-parametric Kruskal-Wallis ANOVA test on untransformed size of FSB+ plaques, $\chi^2 = 4.8$. $p = 0.19$). We also did not detect any differences for plaque sizes across regions for the deep layers (Fig. 2D; PrL, $273.0 \pm 0.4\ \mu m^2$, $n = 914$ plaques; Cg, $277.4 \pm 0.4\ \mu m^2$, $n = 1209$ plaques; M2, $269.2 \pm 0.3\ \mu m^2$, $n = 1358$ plaques; S1, $247.6 \pm 0.4\ \mu m^2$, $n = 782$ plaques; Non-parametric Kruskal-Wallis ANOVA test on untransformed size of FSB+ plaques, $\chi^2 = 4.2$. $p = 0.24$).

We also examined total plaque area, a measure of plaque burden. For superficial layers, there was a significant effect of region (Fig. 2E; PrL, $1.2 \pm 0.3\%$; Cg, $1.3 \pm 0.3\%$; M2, $1.6 \pm 0.3\%$; S1, $0.5 \pm 0.2\%$; One-way ANOVA with brain region as a within subjects factor, $F(3) = 3.8$, $p = 0.03$. *Post-hoc* Tukey-Kramer tests: PrL versus Cg, $p = 0.99$; PrL versus M2, $p = 0.68$; PrL versus S1, $p = 0.02$; Cg versus M2, $p = 0.85$; Cg versus S1, $p = 0.27$; M2 versus S1, $p = 0.06$). Overall, frontal regions have larger plaque burdens. There was also a significant effect of region in the deep layers (Fig. 2F; PrL, $3.2 \pm 0.4\%$; Cg, $4.5 \pm 0.5\%$; M2, $5.3 \pm 0.3\%$; S1, $2.8 \pm 0.4\%$; One-way ANOVA with brain region as a within subjects factor, $F(3) = 10.6$, $p = 1 \times 10^{-4}$. *Post-hoc* Tukey-Kramer tests: PrL versus Cg, $p = 0.26$; PrL versus M2, $p = 0.009$; PrL versus S1, $p = 0.88$; Cg versus M2, $p = 0.13$; Cg versus S1, $p = 0.06$; M2 versus S1, $p = 0.003$). The most prominent effect was the larger plaque burden in M2 and Cg compared to S1. In summary, there is significant regional and laminar vulnerability to plaque burden in 5xFAD mice with deep layer frontal regions being the most susceptible.

### *4G8+ Aβ aggregations*

We additionally analyzed other forms of Aβ aggregation by quantifying 4G8+ Aβ staining. There were extensive amounts 4G8+ Aβ ROIs identified in the four regions analyzed. However, for superficial layers, the different regions did not differ statistically in density of 4G8+ Aβ ROIs (Fig. 3A; PrL, $1.0 \times 10^4 \pm 0.4 \times 10^4$ 4G8+ Aβ ROIs per $mm^2$; Cg, $0.4 \times 10^4 \pm 0.2 \times 10^4$ 4G8+ Aβ ROIs per $mm^2$; M2, $0.5 \times 10^4 \pm 0.3 \times 10^4$ 4G8+ Aβ ROIs per $mm^2$; S1, $0.2 \times 10^4 \pm 0.6 \times 10^3$ 4G8+ Aβ ROIs per $mm^2$; One-way ANOVA with brain region as a within subjects factor, $F(3) = 2.8$, $p = 0.10$). There was also no statistically significant effect of region in the deep layers (Fig. 3B; PrL, $1.3 \times 10^4 \pm 0.4 \times 10^4$ 4G8+ Aβ ROIs per $mm^2$; Cg, $0.9 \times 10^4 \pm 0.5 \times 10^4$ 4G8+ Aβ ROIs per $mm^2$; M2, $0.9 \times 10^4 \pm 0.4 \times 10^4$ 4G8+ Aβ ROIs per $mm^2$; S1, $0.7 \times 10^4 \pm 0.5 \times 10^4$ 4G8+ Aβ ROIs per $mm^2$; One-way ANOVA with brain region as a within subjects factor, $F(3) = 2.9$, $p = 0.9$). Overall, despite the ubiquity of 4G8+ Aβ, there was no region-specific effect.

Sizes of the 4G8+ Aβ were on average very small, on the order of a few $\mu m^2$. The distribution was non-normal and heavy-tailed: most 4G8+ Aβ ROIs were very small with rare large ones (Fig. 3C, D; note the log-transformed x-axis). There was a statistically significant effect of region in the superficial layers (Fig. 3C; PrL, $3.8 \pm 1.3\ \mu m^2$; Cg, $3.1 \pm 0.8\ \mu m^2$; M2, $2.4 \pm 0.4\ \mu m^2$; S1, $1.8 \pm 0.03\ \mu m^2$; Non-parametric Kruskal-Wallis ANOVA test on untransformed size of 4G8+ Aβ, $\chi^2 = 105.0$, $p = 1 \times 10^{-22}$). *Post-hoc* Wilcoxon rank sum test generally revealed PrL as having the largest 4G8+ Aβ sizes (PrL versus Cg, $p = 0.35$; PrL versus M2, $p = 5 \times 10^{-17}$; PrL versus S1, $p = 0.03$; Cg versus M2, $p = 1 \times 10^{-14}$; Cg versus S1, $p = 0.15$; M2 versus

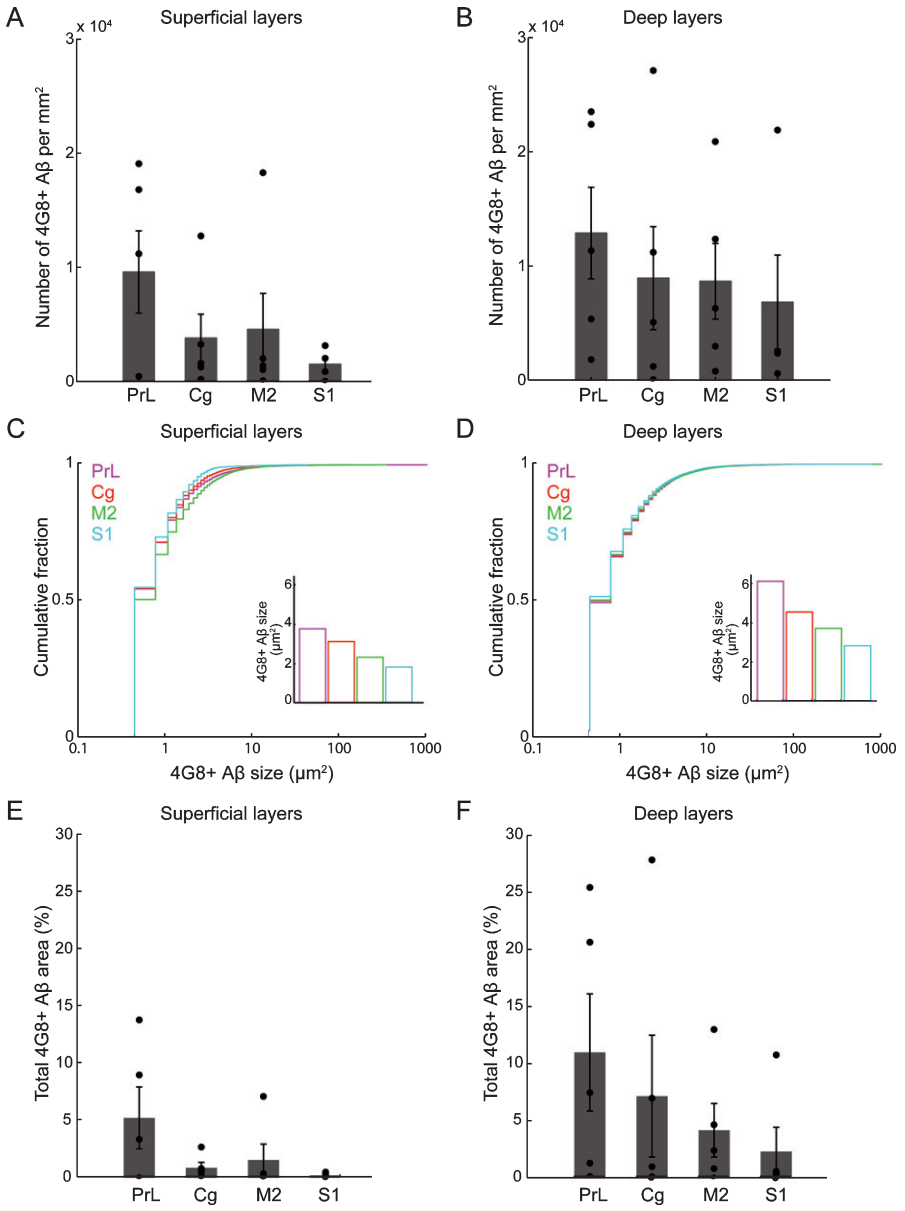


Fig. 3. Laminar and regional distribution of 4G8+ Aβ. A) Number of 4G8+ Aβ per mm$^2$ of superficial layers in each brain region examined. B) Same as (A) but for deep layers. C) Cumulative fraction of absolute size of all 4G8+ Aβ (log10-transformed) analyzed as a function of superficial layers in each brain region examined. Inset, mean 4G8+ Aβ plaque size. D) Same as (C) but for deep layers. E) Total 4G8+ Aβ area as a percentage of superficial layers in each brain region examined. F) Same as (E) but for deep layers. Filled circle, individual animal. Bar, mean ± s.e.m.

S1, $p = 1 \times 10^{-13}$). For deep layers, there was also a statistically significant effect of region (Fig. 3D; PrL, $6.2 \pm 1.3\,\mu m^2$; Cg, $4.6 \pm 0.8\,\mu m^2$; M2, $3.8 \pm 0.4\,\mu m^2$; S1, $2.9 \pm 0.02\,\mu m^2$; Non-parametric Kruskal-Wallis ANOVA test on untransformed size of 4G8+ Aβ, $\chi^2 = 33.7$. $p = 2 \times 10^{-7}$). *Post-hoc* tests similarly revealed PrL as having the largest 4G8+ Aβ sizes (PrL versus Cg, $p = 0.03$; PrL versus M2, $p = 0.004$; PrL versus S1, $p = 1 \times 10^{-8}$; Cg versus M2, $p = 0.46$; Cg versus S1, $p = 1 \times 10^{-4}$; M2 versus S1, $p = 0.001$).

Analyzing total 4G8+ Aβ area (%), a measure of Aβ burden, we did not find any statistically significant effect of region in either superficial (Fig. 3E; PrL, $5.3 \pm 2.7\%$; Cg, $1.0 \pm 0.5\%$; M2, $1.6 \pm 1.4\%$; S1, $0.3 \pm 0.1\%$; One-way ANOVA with brain region

as a within subjects factor, $F(3) = 2.0$, $p = 0.17$) or deep layers (Fig. 3F; PrL, $11.2 \pm 5.1\%$; Cg, $7.3 \pm 5.3\%$; M2, $4.3 \pm 2.3\%$; S1, $3.1 \pm 2.3\%$; One-way ANOVA with brain region as a within subjects factor, $F(3) = 0.9$, $p = 0.47$). To rule out potential confounds of AβPP staining, we re-analyzed the data excluding intracellular 4G8 staining. Consistent with a previous study of 4G8 staining in 5xFAD mice older than 4 months [45], the vast majority of 4G8+ Aβ was extracellular (PrL: $99 \pm 1\%$; Cg: $98 \pm 2\%$; M2:$89 \pm 1\%$; S1:$93 \pm 1\%$). Consequently, the same pattern of results was obtained when analyzing intracellular-excluded 4G8+ Aβ (Supplementary Figure 2). In summary, despite the significant regional and laminar differences in plaque deposits in 5xFAD mice as analyzed above, we did not detect statistical differences in measures of 4G8+ Aβ. This may be due to the larger variability in 4G8+ Aβ staining across animals.

*PV neurons*

We next analyzed PV neuron density as a function of regions, layers, and genotypes. For superficial layers, there was no statistically significant effect of genotype (Fig. 4A; PrL, $45 \pm 14$ neurons per mm$^2$ for WT versus $24 \pm 5$ neurons per mm$^2$ for 5xFAD; Cg, $65 \pm 17$ neurons per mm$^2$ for WT versus $46 \pm 8$ neurons per mm$^2$ for 5xFAD; M2, $131 \pm 38$ neurons per mm$^2$ for WT versus $100 \pm 28$ neurons per mm$^2$ for 5xFAD; S1, $142 \pm 28$ neurons per mm$^2$ for WT versus $84 \pm 10$ neurons per mm$^2$ for 5xFAD; Two-way ANOVA with genotype (WT, 5xFAD) as between-subjects factor and brain regions as within-subjects factor, Genotype effect, $F(1) = 3.2$, $p = 0.10$. Region effect, $F(3) = 11.9$, $p = 9 \times 10^{-5}$. Genotype × region interaction effect, $F(3) = 0.57$, $p = 0.64$).

For deep layers, there was a significant effect of genotype (Fig. 4B; PrL, $154 \pm 8$ neurons per

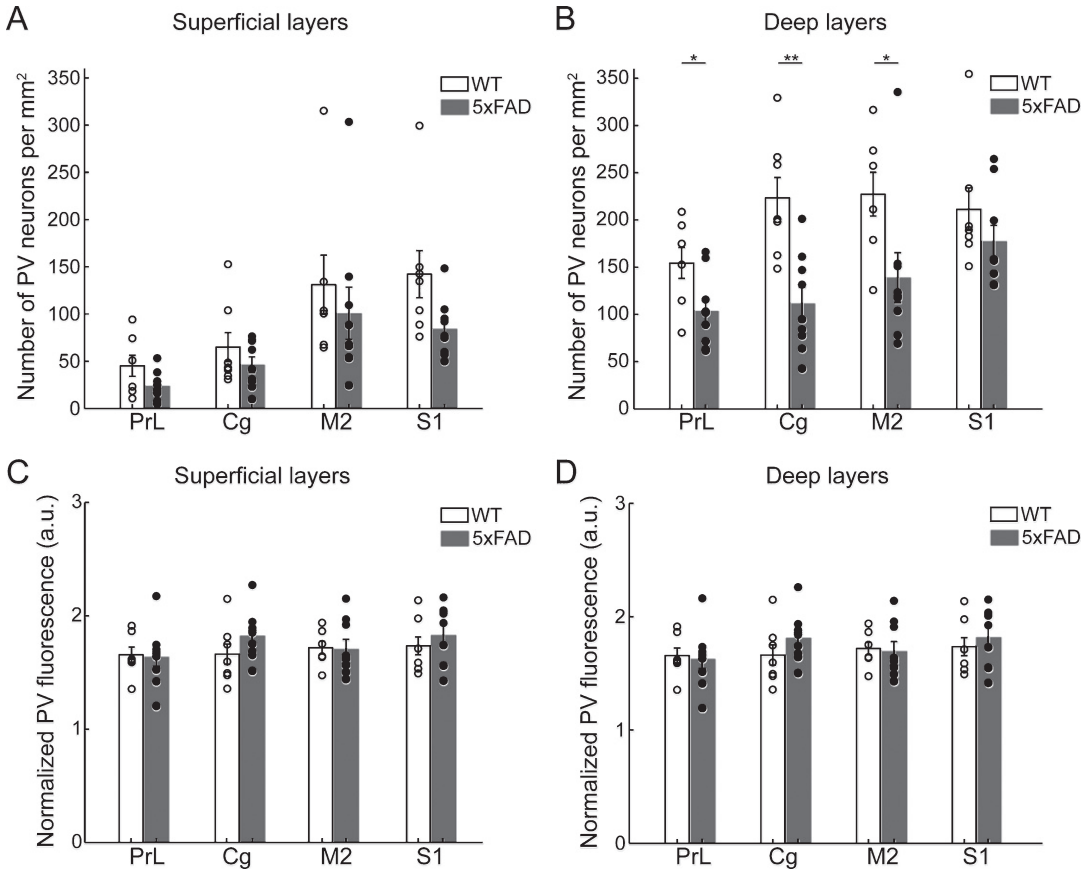


Fig. 4. Laminar and regional distribution of PV neuron density and fluorescence signal as a function of genotypes. A) Number of PV neurons per mm$^2$ in superficial layers of each brain region examined for WT and 5xFAD. B) Same as (A) but for deep layers. C) Normalized PV cell body fluorescence signal per cell in superficial layers each brain region examined for WT and 5xFAD. D) Same as (C) but for deep layers. Filled circle, individual animal. Bar, mean ± s.e.m. $*p < 0.05$; $**p < 0.01$.

$mm^2$ (mean ± SEM) for WT versus 104 ± 4 neurons per $mm^2$ for 5xFAD; Cg, 224 ± 9 neurons per $mm^2$ for WT versus 112 ± 6 neurons per $mm^2$ for 5xFAD; M2, 227 ± 12 neurons per $mm^2$ for WT versus 139 ± 9 neurons per $mm^2$ for 5xFAD; S1, 211 ± 10 neurons per $mm^2$ for WT versus 177 ± 6 neurons per $mm^2$ for 5xFAD; Two-way ANOVA performed as above: Genotype effect, $F(1) = 11.7$, $p = 0.004$. Region effect, $F(3) = 5.6$, $p = 0.002$. Genotype × region interaction effect, $F(3) = 2.1$, $p = 0.11$). The three frontal regions PrL, Cg, and M2 showed a statistically significant reduction of PV density, at –32%, –50%, and –39%, respectively, in 5xFAD animals relative to WT littermate controls (*Post-hoc* Tukey-Kramer tests comparing WT versus 5xFAD for PrL, $p = 0.03$; Cg, $p = 0.002$; M2, $p = 0.03$; S1, $p = 0.27$). Overall, the data suggest regional and laminar vulnerabilities with deep layer PV neurons in frontal regions of 5xFAD animals showing the greatest reductions compared to WT animals.

A reduction in PV neuron density could also result from a reduction in PV expression to below our detection threshold. To test whether there were reductions in PV expression, we analyzed the background-normalized fluorescence of PV cell bodies across genotype (see Materials and Methods). We did not detect any difference between 5xFAD and WT mice in the normalized fluorescence signals per cell body in superficial layers for all four regions (Fig. 4C; Two-way ANOVA with genotype (WT, 5xFAD) as between-subjects factor and brain regions as within-subjects factor, Genotype effect, $F(1) = 0.27$, $p = 0.61$. Region effect, $F(3) = 1.7$, $p = 0.17$. Genotype × region interaction effect, $F(3) = 1.03$, $p = 0.39$). Likewise, we did not observe any difference for PV fluorescence signal per cell in the deep layers (Fig. 4D; Genotype effect, $F(1) = 0.67$, $p = 0.43$. Region effect, $F(3) = 0.95$, $p = 0.42$. Genotype × region interaction effect, $F(3) = 1.22$, $p = 0.31$).

### *Relationship between PV neuron density, FSB+ plaques, and 4G8+ Aβ aggregations*

To investigate the relationship between PV neuron density and Aβ pathology, we correlated PV neuron density with the 3 indicators of FSB+ plaques in the 5xFAD animals: number of plaques per $mm^2$, plaque size (μm), and plaque area (%). We focused on the deep layers given the statistically significant reduction in PV neuron density compared to WT. For PV neurons, we averaged across 5xFAD animals and compared it the average of WT animals to obtain the fractional reduction within each region. We then correlated this measure with each of the indicators of plaque pathology averaged within each region in 5xFAD animals. There was a trend for regions with higher density of FSB+ plaques to exhibit greater reductions in PV neuron density of 5xFAD mice relative to WT ($r = –0.66$, $p = 0.34$; Fig. 5A). However, this negative correlation was not statistically significant due to the small number of regions examined. Similar tendencies held for the other two measures of plaque size ($r = –0.77$, $p = 0.23$; Fig. 5B) and total plaque area ($r = –0.73$, $p = 0.27$; Fig. 5C). We repeated the same analysis for 4G8+ Aβ and found much smaller negative correlations between indicators of 4G8+ Aβ and PV neuron density reductions with none of the correlations being statistically significant (density, $r = –0.29$, $p = 0.71$; size, $r = –0.43$, $p = 0.57$; area, $r = –0.39$, $p = 0.62$; Fig. 5D-F). Overall, though we did not detect statistical significance, there is a tendency for regions with greater Aβ pathology to exhibit more PV neuron loss.

### *In vivo PV neuron loss*

To further confirm the loss of PV neurons, we performed longitudinal two-photon imaging. Using a double transgenic 5xFAD/PV-Cre mouse line combined with viral-mediated Cre-dependent labeling of PV neurons, we tracked the same set of PV neurons *in vivo* for 4 weeks (Fig. 6A, B). The specificity of Cre-dependent expression in cortical PV neurons is > 90% as quantified by other groups using immunohistochemistry [46, 47] and electrophysiology [15, 48]. We imaged the dorsal aspect of the medial prefrontal cortex, encompassing both Cg1 and M2, which were the two regions showing the largest reductions in PV neuron density based on histological assessment. We found multiple instances of PV neurons disappearing *in vivo* in mice harboring the 5xFAD mutations (Fig. 6C). In a few cases, we observed intermediate structures, before all remnants of the neuron fully disappeared in the next timepoint (Fig. 6C, arrows). Overall, across the 4-week period, 88% of the PV neurons that were tracked in 5xFAD/PV-Cre animals survived ($n = 107$ out of 122 neurons, 4 animals; Fig. 6D). In control PV-Cre animals, all of the cells could be tracked for the duration of the experiment ($n = 123$ out of 123 neurons, 4 animals). These results corroborate the histological data to support the notion of PV neuron loss in the frontal cortex of the AD mouse model.

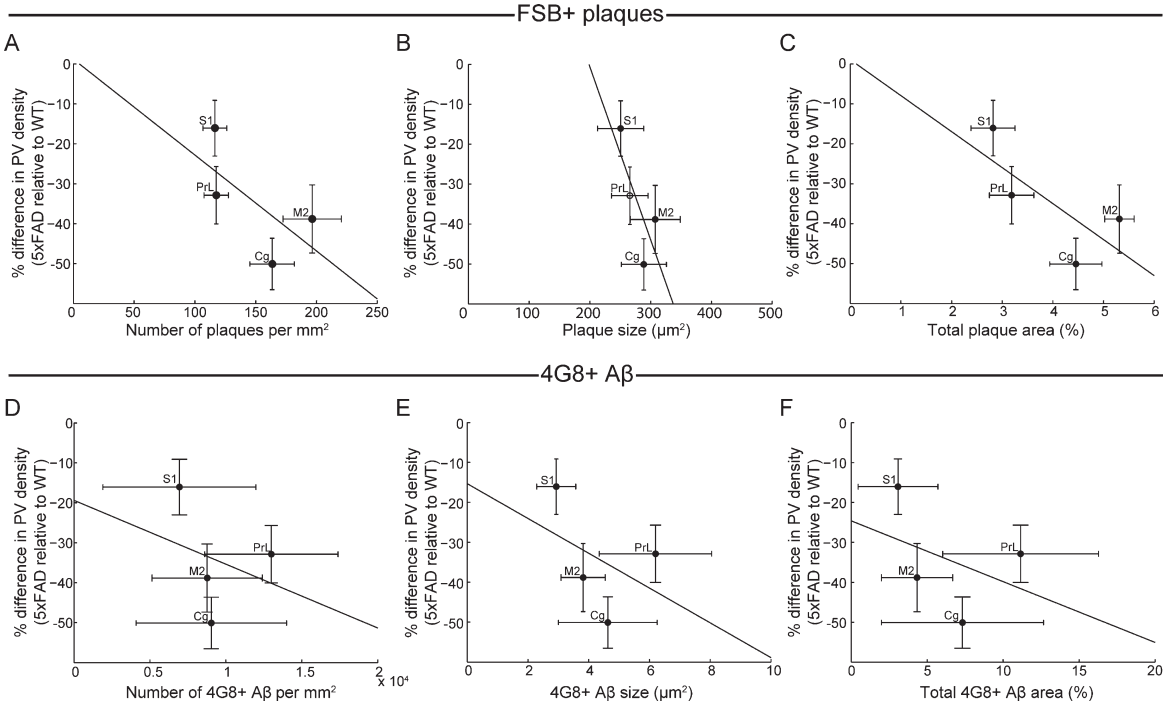


Fig. 5. Relationship between PV neuron density, FSB+ plaques, and 4G8+ Aβ in deep layers. A) Scatterplot of percent difference in PV neuron density (5xFAD relative to WT) against number of plaques per mm$^2$ in deep layers. Each crosshair is the mean ± SEM across animals for the labeled region. Line, best fit least-squares regression line. B) Same as (A) but for plaque size. C) Same as (A) but for total plaque area. D) Scatterplot of percent difference in PV neuron density (5xFAD relative to WT) against number of 4G8+ Aβ per mm$^2$ in deep layers. Each crosshair is the mean ± SEM across animals for the labeled region. Line, best fit least-squares regression line. E) Same as (D) but for 4G8+ Aβ size. F) Same as (D) but for total 4G8+ Aβ area.

## DISCUSSION

Using immunofluorescence staining of brain sections, we characterized Aβ aggregation in multiple regions of the neocortex of 5xFAD mice. We found significant differences in regional and laminar vulnerability to plaque deposits with deep layers of frontal regions, particularly Cg and M2, being most affected. We also found more pronounced PV neuronal loss in the deep layers of frontal regions in 5xFAD mice, again with Cg and M2 being more strongly affected. The regional differences are consistent with the idea that regions with greater Aβ pathology have greater PV neuron loss compared to WT. In the following, we will discuss our results in the context of findings from the 5xFAD mouse model and bring in results from other transgenic lines and human data when relevant. We will speculate on the potential mechanisms for PV neuronal death and propose how this may have severe effects on cortical functions.

The 5xFAD mouse is a widely used model, but a quantitative assessment of within- and across-region distributions of Aβ plaque deposits in this mouse model was lacking. Previous studies have been either qualitative examinations of images [23, 49] or quantitative assessments of large undifferentiated regions (e.g., cortex or hippocampus) [50–53]. Our study suggests significant differences in regional and laminar vulnerability to Aβ plaque deposits (Fig. 2). Two recent studies used whole-brain imaging to characterize Aβ plaque deposits in other transgenic mouse models and found significant regional heterogeneity [54, 55]. However, their study identified different regions as being prone to Aβ plaque deposits compared to ours. Aβ plaque density was the highest in the visual cortical areas for Tg2576, whereas it was retrosplenial cortex for hAPP-J20, and S1 for APPswe/PSEN1dE9 mice. All these mouse lines differ in terms of the mutations and promoters associated with the transgenes, as well as the age of onset for amyloid aggregation, which may explain the different patterns of regional pathology.

Our results suggest that the pattern of amyloid deposits in the 5xFAD model seems to reflect the

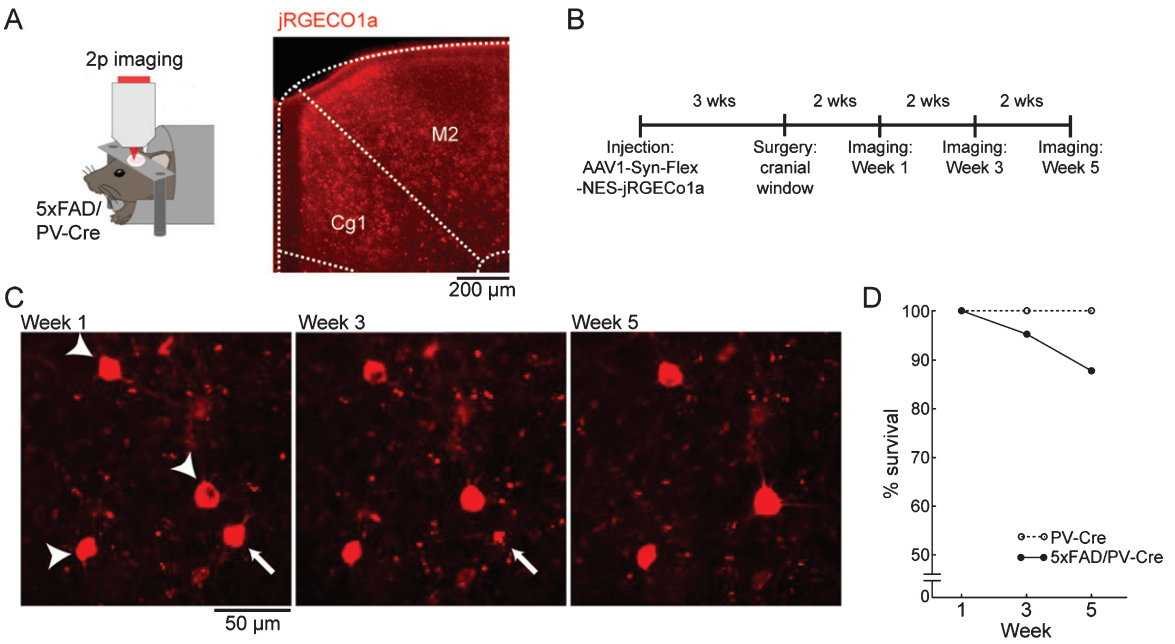


Fig. 6. Longitudinal *in vivo* imaging of PV neurons. A) Left, schematic of *in vivo* two-photon imaging in 5xFAD/PV-Cre animal. Right, histological verification of jRGECO1a expression in Cg1 and M2. Cg1, cingulate cortex area 1; M2, secondary motor area. B) Timeline of surgeries and longitudinal imaging experiments. C) Example *in vivo* field of view of jRGECO1a-expressing PV neurons in a 5xFAD/PV-Cre animal. Arrowheads, neurons observed in all imaging sessions. Arrow, a neuron that was present at Week 1 but was not observed subsequently. D) Survival plot of PV neurons in PV-Cre and 5xFAD/PV-Cre animals.

progression of Aβ pathology in humans, at least in the cortex. Based on a large sample of postmortem brains, three stages of Aβ deposition were identified [1]. The first stage involved the earliest deposits in the cortical association regions whereas primary motor and sensory cortical regions were spared. Only in the third stage were there significant deposits in motor and sensory regions. For the age group that we examined (6–9 months), we observed more Aβ deposits in the frontal association regions than in primary somatosensory region, S1, qualitatively similar to an early frontal vulnerability to Aβ deposition in humans.

We found an interesting pattern of plaque deposits in M2 of the mouse. M2 is an association cortical region that has both sensory- and motor-related correlates and is argued to be important for behavioral flexibility [56]. M2 has the densest plaque counts by 53% and 40% in the superficial (Fig. 2A) and deep layers (Fig. 2B) respectively, compared to the average values from the other frontal regions of PrL and Cg. However, all 3 regions have statistically similar distribution of plaque sizes (Fig. 2C, D). Plaque counts likely reflect the rate of initiation of plaques while plaque sizes represent the growth of already-formed deposits [57, 58]. This large number of plaques initiated in M2 might indicate a selective vulnerability for the seeding of plaques in M2. Plaques are thought to be seeded in a two-stage process with the initial nucleation seed dependent on Aβ peptide concentrations followed by subsequent fibrillar polymerization [59]. Whether our data in M2 is consistent with regional differences in Aβ peptide concentrations is unclear. Regardless, *in vivo* longitudinal imaging specifically in M2 would be informative to understand plaque initiation and growth together with the associated modifications to the neural architecture [60].

Why certain parts of the brain are ultimately more vulnerable to Aβ deposition is a hotly debated question [61]. One possibility is that certain parts of the brain are susceptible due to the high levels of baseline neural activity [62]. Animal studies provide causal evidence to show that prolonged upregulation of neural activity would increase Aβ peptide concentrations and plaque deposits [27, 63]. This putative mechanism fits our observations because, in the mouse, Cg and M2 are part of the default-mode network [64]. The default-mode network in human is highly active while subjects are at rest with no explicit task [65].

Indeed, this network exhibits substantial Aβ load in AD patients [62].

In addition to plaques, we also examined PV neuron density. One previous study in 12-month 5xFAD animals found a ∼29% reduction of PV neuron density in layer 4 of S1 compared to controls but not in layer 5 [66]. However, no comparison was made to superficial layers nor to other regions. In our data, we observed significant regional and laminar differences in PV neuron losses. Deep layers of Cg, M2, and PrL were particularly vulnerable with significant reductions in PV neuron density in 5xFAD mice compared to WT controls: –50%, –39%, and –32% respectively (Fig. 4B). On one hand, our results are consistent with studies of other mouse models that found reductions in PV-immunoreactive neuron density in the piriform and entorhinal cortices [67], as well as in CA1 and CA2 of the hippocampus [68]. Our findings also agree with the reports of AD-related PV neurodegeneration in humans [16–18]. On the other hand, we should note that several other studies have reported no change in PV neuron density in either the neocortex [69, 70] or elsewhere [71, 72]. None of these studies investigated the 5xFAD model, thus it is difficult to compare the results directly. Moreover, our results indicate regional heterogeneity, which may explain the differences across studies because different regions were examined. Furthermore, PV interneurons are not homogeneous, and may be further divided into subtypes such as Chandelier and basket cells. These subtypes have distinct axonal arborizations, and may be preferentially found in different cortical layers [15, 73]. The larger loss of deep-layer PV interneurons may be driven in part by preferential susceptibility to AD pathology for subtypes of PV interneurons.

How does the PV neuronal loss compare to overall loss of neurons in the 5xFAD mouse? Based on a prior study using Nissl staining, there is a reduction of ∼15% in the overall number of cortical neurons in layer 5 of 9-month old 5xFAD mice related to WT [24]. Comparing the fractional differences, this loss is smaller than the loss of deep frontal cortical PV neurons reported in our study. Interestingly, even if we compare older 5xFAD mice at 12 months of age, the loss of layer 5 cortical neurons (∼25%) [24] is still less than what we found for the PV neuronal loss in 6–9-month-old mice in this study. Therefore, compared to the entire neuronal population, PV neurons may be particularly vulnerable to Aβ-related pathology in 5xFAD mice.

We report a loss of PV neurons, but could that be due to a reduction in PV expression rather than cell death? There are two reasons why we believe the results are driven by a loss of PV neurons. First, if the expression of PV is altered by the pathology, we should see differences in the intensity of fluorescent signals per cell body between 5xFAD and WT mice. Instead, there was no detectable difference in the neuronal cell body fluorescence signals in our analysis (Fig. 4C, D). Second, we complemented immunostaining methods with *in vivo* imaging to longitudinally track PV neurons in live mice (Fig. 6). About 12% of the PV neurons were lost over a course of 4 weeks in 5xFAD/PV-Cre animals compared to none in control animals. The loss detected by *in vivo* imaging is less than the fractional reduction found in histology. This could be because our *in vivo* imaging tracked superficial layer 2/3 neurons, and was limited to a 4-week duration. Altogether, these results are consistent with the loss of frontal cortical PV neurons in 5xFAD mice.

We assessed whether there was a relationship between indicators of Aβ pathology and PV neuron density. In our study, when averaging all animals within each region in the deep layers, regions with greater indicators of plaque pathology had greater reductions in PV neuron density compared to WT. Statistical analyses were not informative due to the small number of regions examined. A previous study found a similar negative correlation within the hippocampus but not in the neocortex [74]. Whether regional vulnerability to PV neuron loss is due to the same mechanisms as regional vulnerability to plaque deposits is unclear. More work is needed to determine the cellular and circuit factors that may converge to generate differential vulnerability in the frontal cortex to AD pathology.

The present study has several limitations. One major limitation is that we used 2-D counting methods instead of stereology which can theoretically be unbiased [75]. In practice, both 2-D and 3-D methods have their caveats and we did not explicitly compare the two methods here [76]. Second, we used a 4G8 antibody that can potentially cross-react with precursor forms including intracellular AβPP. This concern is mitigated in our experimental conditions involving pre-treatment of sections and older mice that appear to substantially reduce AβPP staining. This was confirmed by the minimal change in results when we excluded intracellular staining in our analysis. Nonetheless, additional experiments involving other Aβ antibodies may be important. Finally, we

have focused on our study on several key sub-regions of the frontal cortex. Future studies can benefit from a whole-brain assessment as recently done in other mouse models [54, 55].

What are the potential mechanisms for the loss of PV neurons? The loss of PV neurons might be an indirect consequence of the loss of other neurons, particularly pyramidal cells that are the major neuronal population in the cortex and provide excitatory inputs to PV neurons. The loss of innervation onto PV neurons might initiate a cascade that eventually causes PV neuronal death, as recently proposed for neurodegenerative diseases [77]. Alternatively, more directly, Aβ oligomers, which are significantly elevated in 5xFAD mice [78, 79], may induce cytotoxicity within PV interneurons. These potential indirect and direct mechanisms of PV neuron loss are not mutually exclusive and may act in concert.

The loss of PV neurons is expected to affect cortical network function [80]. PV neurons exert perisomatic inhibition onto excitatory neurons and are suggested to be a key component of feedforward and feedback inhibitory circuits [81], gamma band oscillations [82], and sensory perceptual systems [83]. Indeed, previous studies of various AD mouse models have found evidence of dysfunction in each of these circuit-level functions [84–86], though the extent to which they are specifically related to PV neuron-related inhibition versus other forms of inhibition remain to be established. The layer-specific loss of PV neurons reported here has implications on inter-laminar communication. PV neurons generally innervate other neurons locally within ∼200 μm [87]. The selective loss of PV neurons in the deep layers and less so in the superficial layers may affect the timing and extent of information flow within and across cortical layers, potentially affecting inter-laminar-dependent cognitive functions in AD [88]. Finally, a number of *in vivo* imaging studies using mouse models have identified excitatory-inhibitory imbalance in cellular activity in layer 2/3 of the cortex [89–91]. Our finding of layer-specific PV neuron loss thus highlights the need to examine cortical dysfunction in AD in finer details both in terms of cortical regions and laminar specificity.

## ACKNOWLEDGMENTS

We thank A. Nairn for making available the confocal microscope, C. Duman for technical help with the microscope, J. Grutzendler for providing breeder mice, and P. Yuan for technical advice. This work was supported by National Institute of Mental Health grant R01MH112750 (A.C.K.), National Institute on Aging grant P50AG047270 (A.C.K.), Alzheimer's Association Research Fellowship AARF-17-504924 (F.A.), and James Hudson Brown-Alexander Brown Coxe Postdoctoral Fellowship (F.A.).

Authors' disclosures available online (https://www.j-alz.com/manuscript-disclosures/18-1190r4).

## SUPPLEMENTARY MATERIAL

The supplementary material is available in the electronic version of this article: http://dx.doi.org/10.3233/JAD-181190.

## REFERENCES

[1] Braak H, Braak E (1991) Neuropathological stageing of Alzheimer-related changes. *Acta Neuropathol* **82**, 239-259.

[2] Arnold SE, Hyman BT, Flory J, Damasio AR, Van Hoesen GW (1991) The topographical and neuroanatomical distribution of neurofibrillary tangles and neuritic plaques in the cerebral cortex of patients with Alzheimer's disease. *Cereb Cortex* **1**, 103-116.

[3] Klunk WE, Engler H, Nordberg A, Wang Y, Blomqvist G, Holt DP, Bergström M, Savitcheva I, Huang GF, Estrada S (2004) Imaging brain amyloid in Alzheimer's disease with Pittsburgh Compound-B. *Ann Neurol* **55**, 306-319.

[4] Rowe CC, Ng S, Ackermann U, Gong SJ, Pike K, Savage G, Cowie T, Dickinson K, Maruff P, Darby D (2007) Imaging β-amyloid burden in aging and dementia. *Neurology* **68**, 1718-1725.

[5] Brun A, Englund E (1981) Regional pattern of degeneration in Alzheimer's disease: Neuronal loss and histopathological grading. *Histopathology* **5**, 549-564.

[6] Frisoni GB, Pievani M, Testa C, Sabattoli F, Bresciani L, Bonetti M, Beltramello A, Hayashi KM, Toga AW, Thompson PM (2007) The topography of grey matter involvement in early and late onset Alzheimer's disease. *Brain* **130**, 720-730.

[7] Gómez-Isla T, Hollister R, West H, Mui S, Growdon JH, Petersen RC, Parisi JE, Hyman BT (1997) Neuronal loss correlates with but exceeds neurofibrillary tangles in Alzheimer's disease. *Ann Neurol* **41**, 17-24.

[8] Arendt T, Bigl V, Tennstedt A, Arendt A (1984) Correlation between cortical plaque count and neuronal loss in the nucleus basalis in Alzheimer's disease. *Neurosci Lett* **48**, 81-85.

[9] Mann DM, Yates PO, Marcyniuk B (1985) Correlation between senile plaque and neurofibrillary tangle counts in cerebral cortex and neuronal counts in cortex and subcortical structures in Alzheimer's disease. *Neurosci Lett* **56**, 51-55.

[10] Giannakopoulos P, Hof PR, Kövari E, Vallet PG, Herrmann FR, Bouras C (1996) Distinct patterns of neuronal loss and Alzheimer's disease lesion distribution in elderly individuals older than 90 years. *J Neuropathol Exp Neurol* **55**, 1210-1220.

[11] Sasaki H, Muramoto O, Kanazawa I, Arai H, Kosaka K, Iizuka R (1986) Regional distribution of amino acid transmitters in postmortem brains of presenile and senile dementia of Alzheimer type. *Ann Neurol* **19**, 263-269.

[12] Shimohama S, Taniguchi T, Fujiwara M, Kameyama M (1988) Changes in benzodiazepine receptors in alzheimer-type dementia. *Ann Neurol* **23**, 404-406.

[13] Fukuchi K, Hashikawa K, Seiki Y, Moriwaki H, Oku N, Ishida M, Fujita M, Uehara T, Tanabe H, Kusuoka H (1997) Comparison of iodine-123-iomazenil SPECT and technetium-99m-HMPAO-SPECT in Alzheimer's disease. *J Nucl Med* **38**, 467-470.

[14] Meyer M, Koeppe RA, Frey KA, Foster NL, Kuhl DE (1995) Positron emission tomography measures of benzodiazepine binding in Alzheimer's disease. *Arch Neurol* **52**, 314-317.

[15] Jiang X, Shen S, Cadwell CR, Berens P, Sinz F, Ecker AS, Patel S, Tolias AS (2015) Principles of connectivity among morphologically defined cell types in adult neocortex. *Science* **350**, aac9462.

[16] Satoh J, Tabira T, Sano M, Nakayama H, Tateishi J (1991) Parvalbumin-immunoreactive neurons in the human central nervous system are decreased in Alzheimer's disease. *Acta Neuropathol* **81**, 388-395.

[17] Arai H, Emson P, Mountjoy C, Carassco L, Heizmann C (1987) Loss of parvalbumin-immunoreactive neurones from cortex in Alzheimer-type dementia. *Brain Res* **418**, 164-169.

[18] Mikkonen M, Alafuzoff I, Tapiola T, Soininen H, Miettinen R (1999) Subfield-and layer-specific changes in parvalbumin, calretinin and calbindin-D28K immunoreactivity in the entorhinal cortex in Alzheimer's disease. *Neuroscience* **92**, 515-532.

[19] Hof PR, Cox K, Young WG, Celio MR, Rogers J, Morrison JH (1991) Parvalbumin-lmmunoreactive neurons in the neocortex are resistant to degeneration in Alzheimer's disease. *J Neuropathol Exp Neurol* **50**, 451-462.

[20] Sampson VL, Morrison JH, Vickers JC (1997) The cellular basis for the relative resistance of parvalbumin and calretinin immunoreactive neocortical neurons to the pathology of Alzheimer's disease. *Exp Neurol* **145**, 295-302.

[21] Solodkin A, Veldhuizen SD, Van Hoesen GW (1996) Contingent vulnerability of entorhinal parvalbumin-containing neurons in Alzheimer's disease. *J Neurosci* **16**, 3311-3321.

[22] Spires TL, Hyman BT (2005) Transgenic models of Alzheimer's disease: Learning from animals. *NeuroRx* **2**, 423-437.

[23] Oakley H, Cole SL, Logan S, Maus E, Shao P, Craft J, Guillozet-Bongaarts A, Ohno M, Disterhoft J, Van Eldik L, Berry R, Vassar R (2006) Intraneuronal β-amyloid aggregates, neurodegeneration, and neuron loss in transgenic mice with five familial Alzheimer's disease mutations: Potential factors in amyloid plaque formation. *J Neurosci* **26**, 10129-10140.

[24] Eimer WA, Vassar R (2013) Neuron loss in the 5XFAD mouse model of Alzheimer's disease correlates with intraneuronal Aβ 42 accumulation and caspase-3 activation. *Mol Neurodegener* **8**, 2.

[25] Crowe SE, Ellis-Davies GC (2013) *In vivo* characterization of a bigenic fluorescent mouse model of Alzheimer's disease with neurodegeneration. *J Comp Neurol* **521**, 2181-2194.

[26] Crowe SE, Ellis-Davies GC (2014) Spine pruning in 5xFAD mice starts on basal dendrites of layer 5 pyramidal neurons. *Brain Struct Funct* **219**, 571-580.

[27] Yuan P, Grutzendler J (2016) Attenuation of β-amyloid deposition and neurotoxicity by chemogenetic modulation of neural activity. *J Neurosci* **36**, 632-641.

[28] Condello C, Yuan P, Schain A, Grutzendler J (2015) Microglia constitute a barrier that prevents neurotoxic protofibrillar Aβ42 hotspots around plaques. *Nat Commun* **6**, 6176.

[29] Ohno M (2009) Failures to reconsolidate memory in a mouse model of Alzheimer's disease. *Neurobiol Learn Mem* **92**, 455-459.

[30] Fiol-deRoque MA, Gutierrez-Lanza R, Terés S, Torres M, Barceló P, Rial RV, Verkhratsky A, Escribá PV, Busquets X, Rodríguez JJ (2013) Cognitive recovery and restoration of cell proliferation in the dentate gyrus in the 5XFAD transgenic mice model of Alzheimer's disease following 2-hydroxy-DHA treatment. *Biogerontology* **14**, 763-775.

[31] Hippenmeyer S, Vrieseling E, Sigrist M, Portmann T, Laengle C, Ladle DR, Arber S (2005) A developmental switch in the response of DRG neurons to ETS transcription factor signaling. *PLoS Biol* **3**, e159.

[32] Franklin KBJ, Paxinos G (2007) *The mouse brain in stereotaxic coordinates*, Academic Press, New York.

[33] Molgaard S, Ulrichsen M, Boggild S, Holm M-L, Vaegter C, Nyengaard J, Glerup S (2014) Immunohistochemical visualization of mouse interneuron subtypes. *F1000Research* **3**, 242.

[34] Whissell PD, Cajanding JD, Fogel N, Kim JC (2015) Comparative density of CCK-and PV-GABA cells within the cortex and hippocampus. *Front Neuroanat* **9**, 124.

[35] Bayguinov PO, Ma Y, Gao Y, Zhao X, Jackson MB (2017) Imaging voltage in genetically-defined neuronal subpopulations with a Cre recombinase-targeted hybrid voltage sensor. *J Neurosci* **37**, 9305-9319.

[36] Christensen DZ, Bayer TA, Wirths O (2009) Formic acid is essential for immunohistochemical detection of aggregated intraneuronal Aβ peptides in mouse models of Alzheimer's disease. *Brain Res* **1301**, 116-125.

[37] Espada J, Juarranz Á, Galaz S, Cañete M, Villanueva Á, Pacheco M, Stockert JC (2005) Non-aqueous permanent mounting for immunofluorescence microscopy. *Histochem Cell Biol* **123**, 329-334.

[38] Preibisch S, Saalfeld S, Tomancak P (2009) Globally optimal stitching of tiled 3D microscopic image acquisitions. *Bioinformatics* **25**, 1463-1465.

[39] Dana H, Mohar B, Sun Y, Narayan S, Gordus A, Hasseman JP, Tsegaye G, Holt GT, Hu A, Walpita D (2016) Sensitive red protein calcium indicators for imaging neural activity. *Elife* **5**, e12727.

[40] Ali F, Gerhard DM, Sweasy K, Pothula S, Pittenger C, Duman RS, Kwan AC (accepted) Ketamine disinhibits dendrites and enhances calcium signals in prefrontal dendritic spines. *Nat Commun*.

[41] Pologruto TA, Sabatini BL, Svoboda K (2003) ScanImage: Flexible software for operating laser scanning microscopes. *Biomed Eng Online* **2**, 13.

[42] Sato K, Higuchi M, Iwata N, Saido TC, Sasamoto K (2004) Fluoro-substituted and 13C-labeled styrylbenzene derivatives for detecting brain amyloid plaques. *Eur J Med Chem* **39**, 573-578.

[43] Hatami A, Albay R, Monjazeb S, Milton S, Glabe C (2014) Monoclonal antibodies against Aβ42 fibrils distinguish multiple aggregation state polymorphisms *in vitro* and in Alzheimer disease brain. *J Biol Chem* **289**, 32131-32143.

[44] Kayed R, Head E, Sarsoza F, Saing T, Cotman CW, Necula M, Margol L, Wu J, Breydo L, Thompson JL (2007) Fibril specific, conformation dependent antibodies recognize a generic epitope common to amyloid fibrils and fibril-

lar oligomers that is absent in prefibrillar oligomers. *Mol Neurodegener* **2**, 18.

[45] Moon M, Hong H-S, Nam DW, Baik SH, Song H, Kook S-Y, Kim YS, Lee J, Mook-Jung I (2012) Intracellular amyloid-β accumulation in calcium-binding protein-deficient neurons leads to amyloid-β plaque formation in animal model of Alzheimer's disease. *J Alzheimers Dis* **29**, 615-628.

[46] Pinto L, Dan Y (2015) Cell-type-specific activity in prefrontal cortex during goal-directed behavior. *Neuron* **87**, 437-450.

[47] Xie Y, Chen S, Wu Y, Murphy TH (2014) Prolonged deficits in parvalbumin neuron stimulation-evoked network activity despite recovery of dendritic structure and excitability in the somatosensory cortex following global ischemia in mice. *J Neurosci* **34**, 14890-14900.

[48] Kim H, Ährlund-Richter S, Wang X, Deisseroth K, Carlén M (2016) Prefrontal parvalbumin neurons in control of attention. *Cell* **164**, 208-218.

[49] Jay TR, Miller CM, Cheng PJ, Graham LC, Bemiller S, Broihier ML, Xu G, Margevicius D, Karlo JC, Sousa GL (2015) TREM2 deficiency eliminates TREM2+ inflammatory macrophages and ameliorates pathology in Alzheimer's disease mouse models. *J Exp Med* **212**, 287-295.

[50] O'Connor T, Sadleir KR, Maus E, Velliquette RA, Zhao J, Cole SL, Eimer WA, Hitt B, Bembinster LA, Lammich S (2008) Phosphorylation of the translation initiation factor eIF2α increases BACE1 levels and promotes amyloidogenesis. *Neuron* **60**, 988-1009.

[51] Ohno M, Cole SL, Yasvoina M, Zhao J, Citron M, Berry R, Disterhoft JF, Vassar R (2007) BACE1 gene deletion prevents neuron loss and memory deficits in 5XFAD APP/PS1 transgenic mice. *Neurobiol Dis* **26**, 134-145.

[52] Jawhar S, Trawicka A, Jenneckens C, Bayer TA, Wirths O (2012) Motor deficits, neuron loss, and reduced anxiety coinciding with axonal degeneration and intraneuronal Aβ aggregation in the 5XFAD mouse model of Alzheimer's disease. *Neurobiol Aging* **33**, 196.e129-196.e140.

[53] Girard SD, Baranger K, Gauthier C, Jacquet M, Bernard A, Escoffier G, Marchetti E, Khrestchatisky M, Rivera S, Roman FS (2013) Evidence for early cognitive impairment related to frontal cortex in the 5XFAD mouse model of Alzheimer's disease. *J Alzheimers Dis* **33**, 781-796.

[54] Whitesell JD, Buckley AR, Knox JE, Kuan L, Graddis N, Pelos A, Mukora A, Wakeman W, Bohn P, Ho A (2019) Whole brain imaging reveals distinct spatial patterns of amyloid beta deposition in three mouse models of Alzheimer's disease. *J Comp Neurol* **527**, 2122-2145.

[55] Liebmann T, Renier N, Bettayeb K, Greengard P, Tessier-Lavigne M, Flajolet M (2016) Three-dimensional study of Alzheimer's disease hallmarks using the iDISCO clearing method. *Cell Rep* **16**, 1138-1152.

[56] Barthas F, Kwan AC (2017) Secondary motor cortex: Where 'sensory'meets 'motor'in the rodent frontal cortex. *Trends Neurosci* **40**, 181-193.

[57] Burgold S, Filser S, Dorostkar MM, Schmidt B, Herms J (2014) *In vivo* imaging reveals sigmoidal growth kinetic of β-amyloid plaques. *Acta Neuropathol Commun* **2**, 30.

[58] Hefendehl JK, Wegenast-Braun BM, Liebig C, Eicke D, Milford D, Calhoun ME, Kohsaka S, Eichner M, Jucker M (2011) Long-term *in vivo* imaging of β-amyloid plaque appearance and growth in a mouse model of cerebral β-amyloidosis. *J Neurosci* **31**, 624-629.

[59] Harper JD, Lansbury Jr PT (1997) Models of amyloid seeding in Alzheimer's disease and scrapie: Mechanistic truths and physiological consequences of the time-dependent solubility of amyloid proteins. *Annu Rev Biochem* **66**, 385-407.

[60] Phoumthipphavong V, Barthas F, Hassett S, Kwan AC (2016) Longitudinal effects of ketamine on dendritic architecture *in vivo* in the mouse medial frontal cortex. *Eneuro* **3**, ENEURO.0133-15.2016.

[61] Fu H, Hardy J, Duff KE (2018) Selective vulnerability in neurodegenerative diseases. *Nat Neurosci* **21**, 1350-1358.

[62] Buckner RL, Snyder AZ, Shannon BJ, LaRossa G, Sachs R, Fotenos AF, Sheline YI, Klunk WE, Mathis CA, Morris JC (2005) Molecular, structural, and functional characterization of Alzheimer's disease: Evidence for a relationship between default activity, amyloid, and memory. *J Neurosci* **25**, 7709-7717.

[63] Bero AW, Yan P, Roh JH, Cirrito JR, Stewart FR, Raichle ME, Lee J-M, Holtzman DM (2011) Neuronal activity regulates the regional vulnerability to amyloid-β deposition. *Nat Neurosci* **14**, 750.

[64] Stafford JM, Jarrett BR, Miranda-Dominguez O, Mills BD, Cain N, Mihalas S, Lahvis GP, Lattal KM, Mitchell SH, David SV (2014) Large-scale topology and the default mode network in the mouse connectome. *Proc Natl Acad Sci U S A* **111**, 18745-18750.

[65] Whitfield-Gabrieli S, Ford JM (2012) Default mode network activity and connectivity in psychopathology. *Ann Rev Clin Psychol* **8**, 49-76.

[66] Flanigan TJ, Xue Y, Kishan Rao S, Dhanushkodi A, McDonald MP (2014) Abnormal vibrissa-related behavior and loss of barrel field inhibitory neurons in 5xFAD transgenics. *Genes Brain Behav* **13**, 488-500.

[67] Saiz-Sanchez D, Ubeda-Banon I, la Rosa-Prieto D, Martinez-Marcos A (2012) Differential expression of interneuron populations and correlation with amyloid-β deposition in the olfactory cortex of an AβPP/PS1 transgenic mouse model of Alzheimer's disease. *J Alzheimers Dis* **31**, 113-129.

[68] Takahashi H, Brasnjevic I, Rutten BP, Van Der Kolk N, Perl DP, Bouras C, Steinbusch HW, Schmitz C, Hof PR, Dickstein DL (2010) Hippocampal interneuron loss in an APP/PS1 double mutant mouse and in Alzheimer's disease. *Brain Struct Funct* **214**, 145-160.

[69] Lemmens MA, Sierksma AS, Rutten BP, Dennissen F, Steinbusch HW, Lucassen PJ, Schmitz C (2011) Age-related changes of neuron numbers in the frontal cortex of a transgenic mouse model of Alzheimer's disease. *Brain Struct Funct* **216**, 227.

[70] Moreno-Gonzalez I, Baglietto-Vargas D, Sanchez-Varo R, Jimenez S, Trujillo-Estrada L, Sanchez-Mejias E, del Rio JC, Torres M, Romero-Acebal M, Ruano D (2009) Extracellular amyloid-β and cytotoxic glial activation induce significant entorhinal neuron loss in young PS1 M146L/APP 751SL mice. *J Alzheimers Dis* **18**, 755-776.

[71] Albuquerque MS, Mahar I, Davoli MA, Chabot J-G, Mechawar N, Quirion R, Krantic S (2015) Regional and subregional differences in hippocampal GABAergic neuronal vulnerability in the TgCRND8 mouse model of Alzheimer's disease. *Front Aging Neurosci* **7**, 30.

[72] Trujillo-Estrada L, Davila JC, Sanchez-Mejias E, Sánchez-Varo R, Gomez-Arboledas A, Vizuete M, Vitorica J, Gutiérrez A (2014) Early neuronal loss and axonal/presynaptic damage is associated with accelerated amyloid-β accumulation in AβPP/PS1 Alzheimer's disease mice subiculum. *J Alzheimers Dis* **42**, 521-541.

[73] Taniguchi H, Lu J, Huang ZJ (2013) The spatial and temporal origin of chandelier cells in mouse neocortex. *Science* **339**, 70-74.
[74] Calhoun ME, Wiederhold K-H, Abramowski D, Phinney AL, Probst A, Sturchler-Pierrat C, Staufenbiel M, Sommer B, Jucker M (1998) Neuron loss in APP transgenic mice. *Nature* **395**, 755.
[75] Schmitz C, Hof P (2005) Design-based stereology in neuroscience. *Neuroscience* **130**, 813-831.
[76] Benes FM, Lange N (2001) Two-dimensional versus three-dimensional cell counting: A practical perspective. *Trends Neurosci* **24**, 11-17.
[77] Roselli F, Caroni P (2015) From intrinsic firing properties to selective neuronal vulnerability in neurodegenerative diseases. *Neuron* **85**, 901-910.
[78] Ohno M, Chang L, Tseng W, Oakley H, Citron M, Klein WL, Vassar R, Disterhoft JF (2006) Temporal memory deficits in Alzheimer's mouse models: Rescue by genetic deletion of BACE1. *Eur J Neurosci* **23**, 251-260.
[79] Devi L, Ohno M (2015) Effects of BACE1 haploinsufficiency on APP processing and Aβ concentrations in male and female 5XFAD Alzheimer mice at different disease stages. *Neuroscience* **307**, 128-137.
[80] Palop JJ, Mucke L (2016) Network abnormalities and interneuron dysfunction in Alzheimer disease. *Nat Rev Neurosci* **17**, 777.
[81] Isaacson JS, Scanziani M (2011) How inhibition shapes cortical activity. *Neuron* **72**, 231-243.
[82] Sohal VS, Zhang F, Yizhar O, Deisseroth K (2009) Parvalbumin neurons and gamma rhythms enhance cortical circuit performance. *Nature* **459**, 698.
[83] Lee S-H, Kwan AC, Zhang S, Phoumthipphavong V, Flannery JG, Masmanidis SC, Taniguchi H, Huang ZJ, Zhang F, Boyden ES (2012) Activation of specific interneurons improves V1 feature selectivity and visual perception. *Nature* **488**, 379.
[84] Verret L, Mann EO, Hang GB, Barth AM, Cobos I, Ho K, Devidze N, Masliah E, Kreitzer AC, Mody I (2012) Inhibitory interneuron deficit links altered network activity and cognitive dysfunction in Alzheimer model. *Cell* **149**, 708-721.
[85] Iaccarino HF, Singer AC, Martorell AJ, Rudenko A, Gao F, Gillingham TZ, Mathys H, Seo J, Kritskiy O, Abdurrob F (2016) Gamma frequency entrainment attenuates amyloid load and modifies microglia. *Nature* **540**, 230.
[86] Grienberger C, Rochefort NL, Adelsberger H, Henning HA, Hill DN, Reichwald J, Staufenbiel M, Konnerth A (2012) Staged decline of neuronal function *in vivo* in an animal model of Alzheimer's disease. *Nat Commun* **3**, 774.
[87] Packer AM, Yuste R (2011) Dense, unspecific connectivity of neocortical parvalbumin-positive interneurons: A canonical microcircuit for inhibition? *J Neurosci* **31**, 13260-13271.
[88] Opris I, Casanova MF (2014) Prefrontal cortical minicolumn: From executive control to disrupted cognitive processing. *Brain* **137**, 1863-1875.
[89] Bai Y, Li M, Zhou Y, Ma L, Qiao Q, Hu W, Li W, Wills ZP, Gan W-B (2017) Abnormal dendritic calcium activity and synaptic depotentiation occur early in a mouse model of Alzheimer's disease. *Mol Neurodegener* **12**, 86.
[90] Busche MA, Grienberger C, Keskin AD, Song B, Neumann U, Staufenbiel M, Förstl H, Konnerth A (2015) Decreased amyloid-β and increased neuronal hyperactivity by immunotherapy in Alzheimer's models. *Nat Neurosci* **18**, 1725.
[91] Busche MA, Eichhoff G, Adelsberger H, Abramowski D, Wiederhold K-H, Haass C, Staufenbiel M, Konnerth A, Garaschuk O (2008) Clusters of hyperactive neurons near amyloid plaques in a mouse model of Alzheimer's disease. *Science* **321**, 1686-1689.